Ozone Variability Induced by Synoptic Weather Patterns in Warm Seasons of 2014–2018 over the Yangtze River Delta Region, China

Da Gao[1], Min Xie[1*], Jane Liu[2,3], Tijian Wang[1], Chaoqun Ma[1,a], Haokun Bai[1], Xing Chen[1], Mengmeng Li[1], Bingliang Zhuang[1], Shu Li[1]

[1] School of Atmospheric Sciences, Joint Center for Atmospheric Radar Research of CMA/NJU, CMA-NJU Joint Laboratory for Climate Prediction Studies, Jiangsu Collaborative Innovation Center for Climate Change, Nanjing University, Nanjing 210023, China

[2] College of Geographic Sciences, Fujian Normal University, Fuzhou 350007, China

[3] Department of Geography and Planning, University of Toronto M5S 3G3, Canada

[a] now at: Minerva Research Group, Max Planck Institute for Chemistry, Mainz, Germany

---

* Corresponding author. School of Atmospheric Sciences, Nanjing University, Nanjing 210023, China. minxie@nju.edu.cn (M. Xie)

Abstract: Ozone (O_3) pollution is of great concern in the Yangtze River Delta (YRD) region of China, and the regional O_3 pollution is closely associated with dominant weather systems. With a focus on the warm seasons (April–September) from 2014 to 2018, we quantitatively analyze the characteristics of O_3 variations over the YRD, the impacts of large-scale and synoptic-scale circulations on the O_3 variations and the associated meteorological controlling factors, based on observed ground-level O_3 and meteorological data. Our analysis suggests an increasing trend of the regional mean O_3 concentration in the YRD at 1.8 ppb per year over 2014–2018. Spatially, the empirical orthogonal function analysis suggests the dominant mode accounting for 65.7% variation in O_3, implying that an increase in O_3 is the dominant tendency in the entire YRD. Meteorology is estimated to increase the regional mean O_3 concentration by 3.1 ppb at most from 2014 to 2018. Especially, relative humidity (RH) plays the most important role in modulating the inter-annual O_3 variation, followed by solar radiation (SR) and low cloud cover (LCC). As atmospheric circulations can affect local meteorological factors and O_3 levels, we identify five dominant synoptic weather patterns (SWPs) in the warm seasons in the YRD using the t-mode principal component analysis

classification. The typical weather systems of SWPs include the western Pacific Subtropical High (WPSH) under SWP1, a continental high and the Aleutian low under SWP2, an extratropical cyclone under SWP3, a southern low pressure and WPSH under SWP4 and the north China anticyclone under SWP5. The variations of the five SWPs are all favorable to the increase in O_3 concentrations over 2014–2018. However, crucial meteorological factors leading to increases in O_3 concentrations are different under different SWPs. These factors are identified as significant decreases in RH and increases in SR under SWPs 1, 4 and 5, significant decreases in RH, increases in SR and air temperature (T2) under SWP2, and significant decreases in RH under SWP3. Under SWPs 1, 4 and 5, significant decreases in RH and increases in SR are predominantly caused by the WPSH weakening under SWP1, the southern low pressure weakening under SWP4, and the north China anticyclone weakening under SWP5. Under SWP2, significant decreases in RH, increases in SR and T2 are mainly produced by the Aleutian low southward extending and a continental high weakening. Under SWP3, significant decreases in RH is mainly induced by an extratropical cyclone strengthening. These changes in atmospheric circulations prevent the water vapor in the southern and northern sea from being transported to the YRD and result in RH significantly decreasing under each SWP. In addition, strengthened descending motions (behind the strengthening trough and in front of the strengthening ridge) lead to decreases in LCC and significant increases in SR under SWP1, 2, 4 and 5. The significant increases in T2 would be due to weakening cold flow introduced by a weakening continental high. Most importantly, the changes in the SWP intensity can make large variations in meteorological factors and contribute more to the O_3 inter-annual variation than the changes in the SWP frequency. Finally, we reconstruct an EOF mode 1 time series that is highly correlated with the original O_3 time series, and the reconstructed time series performs well in defining the change in SWP intensity according to the unique feature under each of the SWPs.

1. Introduction

As an air pollutant, surface ozone (O_3) is harmful to human health and vegetation growth, such as damaging human lungs (Jerrett et al. 2009; Day et al. 2017) and destroying forest and agricultural crops (Yue et al. 2017). After the emission control following “Thirteenth Five-Year Plan” Comprehensive Work Plan for Energy Saving and Emission Reduction in China since 2016, concentrations of many pollutants have decreased over the past few years in China, but not for O_3.

Furthermore, heavy O_3 pollution episodes occur more frequently and more severely in China than in Japan, South Korea, the United States, and the European countries (Lu et al. 2018). Li et al. (2018) proposed that the rapid decrease of fine particulate matter (PM) in China is a reason for such O_3 increase as aerosol sinks of hydro-preoxy radicals are reduced. Yet, meteorological influences on the O_3 increase are unclear and require further investigations.

Surface O_3 is mainly formed through complex and nonlinear photochemical reactions of volatile organic compounds (VOCs) and nitrogen oxides (NO_x) exposed to the sunlight (Xie et al. 2014). Meteorology can affect O_3 levels through modulation of photochemical reactions, advection, convection and turbulent transport, as well as dry and wet depositions (Liu et al. 2013; Xie et al., 2016a, 2016b). Synoptic weather patterns (SWPs) and the associated meteorological conditions can impact long-term and daily O_3 variations (Hegarty et al. 2007; Santurtún et al. 2015; Gao et al. 2020; Shu et al., 2020). Understanding the mechanisms of meteorological influences on O_3 variations and quantifying such influences would help to understand the formation of O_3 pollution.

Previous studies have revealed that severe O_3 pollution episodes are usually accompanied with high temperature, strong solar radiation, drying condition and stagnant weather (Jacob and Winner 2009; Doherty et al. 2013; Shu et al. 2016; Pu et al. 2017; Zhang et al. 2018), and these local meteorological conditions are often related to specific synoptic-scale and large-scale atmospheric circulation systems (Fiore et al. 2003; Leibensperger et al. 2008; Barnes and Fiore. 2013; Shu et al. 2016; Wang et al. 2016; Zhao and Wang. 2017). For example, O_3 pollution in the eastern United States is notably influenced by the cyclone frequency (Leibensperger et al. 2008), latitude of the polar jet over eastern North America (Barnes and Fiore. 2013) and the behavior of the quasi-permanent Bermuda High (Fiore et al. 2003; Wang et al. 2016). In China, Yang et al. (2014) illustrated that the changes in meteorological variables, associated with the East Asian summer monsoon, lead to 2–5 % inter-annual variations in surface O_3 concentrations over the central-eastern China. Zhao and Wang (2017) found that a significantly strong western Pacific subtropical high (WPSH) could result in higher relative humidity (RH), more clouds, more rainfall, and less ultraviolet radiation, finally leading to less O_3 formation. Using model simulation, Shu et al. (2016) investigated the synergistical impact of the WPSH and typhoons on O_3 pollution in Yangtze River Delta region.

As known, a region is influenced by different weather systems. Weather classification, as a way to distinguish the different large-scale and synoptic-scale atmospheric circulation systems, is widely used in exploring connections between weather patterns and O_3 levels (Han et al. 2020; Gao et al. 2020). Gao et al. (2020) discussed influences of six SWPs on O_3 levels in the YRD, and revealed differences in O_3 pollution levels due to minor changes in atmospheric circulations. However, it is uncertain that how changes in the SWPs could lead to O_3 pollution in detail, especially in the YRD. For the northern China and the PRD region, Liu et al. (2019) quantified the impact of synoptic circulation patterns on O_3 variability in the northern China from April to October during 2013–2017. Yang et al. (2019) quantitatively assessed the impacts of meteorological factors and the precursor emissions on the long-term trend of ambient O_3 over the PRD region. However, whether variations in SWPs can lead to O_3 increases in recent years over the YRD has not be sufficiently addressed.

Due to the recent increases in O_3 level over the YRD (Gao et al. 2017; Xie et al. 2017), studies on characterizing the O_3 variation in the region and understanding the mechanisms for the variation are urgently required. To this end, the temporal and spatial variations in surface O_3 including 5-year trend over the YRD are quantitatively investigated, and the mechanisms of meteorological influences on the O_3 variations are analyzed. Especially, the characteristics of the corresponding SWPs are discussed in detailed. The remainder of this paper is organized as follows. Data and methods are introduced in section 2. The inter-annual variation and 5-year trend and spatial variation characteristics of surface ozone in the YRD are illustrated in section 3.1. The impact of meteorological factors on the O_3 variation is discussed in section 3.2. The main SWPs and the effects of their changes on the O_3 variation are described in section 3.3. Section 3.4 discusses the contributions of the changes in SWP intensity and frequency to the inter-annual variation and trend of O_3. Finally, the conclusion and discussions are shown in section 4.

2. Data and methods

2.1. O_3 and meteorological datasets

The maximum daily 8-hours average O_3 data are available from the National Environmental Monitoring Center of China, which were acquired from the air quality real-time publishing platform (http://106.37.208.233:20035). The hourly observation data of meteorological factors including air temperature (T2), RH and wind speed (WS) in the warm seasons from April to September over

2014–2018 were acquired from the National Meteorological Center of China Meteorological Administration (http://eng.nmc.cn). 26 cities are selected as typical cities representative of the YRD according to the "Urban agglomeration on Yangtze River Delta" approved by China's State Council in 2016. There are total 172 stations in 26 cities. In order to better characterize the O_3 pollution levels of each city, the hourly O_3 concentration of each city is calculated as the average value of the O_3 concentrations measured in several of the national monitoring sites in that city. In this paper, the term "O_3 concentration" refers to the maximum daily 8-hours average O_3 concentration unless stated otherwise.

2.2. Linear trend analyses

To characterize the O_3 variation in the warm seasons during 2014–2018 over the YRD, a linear trend method based on monthly anomalies is used (see Equation 1), which has been widely used to calculate the trends of time series with seasonal cycles and autocorrelation. The O_3 monthly anomalies are more precise than O_3 monthly means because the impact of missing data is reduced. In addition, hourly O_3 data and fewer yearly O_3 data are inappropriate to use because of too many temporal variation signals and easily overfitting. Using this method, Cooper et al. (2020) and Lu et al. (2020) quantified the O_3 trend in 27 globally distributed remote locations and the whole China. Anomalies of monthly average O_3 concentration are defined as the difference between the individual monthly mean and the monthly mean of 2014–2018. The parametric linear trend is calculated by using the generalized least-squares method with auto-regression.

$$y_t = b + kt + \alpha \cos\left(\frac{2\pi M}{6}\right) + \beta \sin\left(\frac{2\pi M}{6}\right) + R_t \qquad (1),$$

where y_t represents the monthly anomaly, t is the monthly index from April to September during 2014–2018, b denotes the intercept, k is the linear trend, α and β are coefficients for a 6-month harmonic series (M ranges from 1 to 6) which is used to account for potentially remaining seasonal signals, and R_t represents a normal random error series. In this study, linear trend k is regarded as the inter-annual O_3 variation trend and is discussed in section 3.1.1.

2.3. Meteorological adjustment

The meteorological adjustment, a statistical method, is applied to quantify the impact of

meteorology on O_3 variation through removing such impact in the original O_3 data. It is similar to a model simulation that keeps the emission levels fixed but allows meteorology to vary. Yet, this method requires much less computing resources than a model simulation. The method is introduced in detail as follows.

In the meteorological adjustment, the observed O_3 and meteorological data are separated into long-term, seasonal, and short-term data (Rao and Zurbenko 1994a, b). The Kolmogorov-Zurbenko (KZ) filter can be expressed as follows.

$$R(t) = L(t) + S(t) + W(t) \quad (2),$$

where $R(t)$ represents the raw time series data, $L(t)$ the long-term trend on a timescale of years, $S(t)$ the seasonal variation on a timescale of months, and $W(t)$ the short-term component on a timescale of days.

In order to remove the high-pass signal, the KZ filter carries out p times of iterations of a moving average with the window length m, which is defined as

$$Y_i = \frac{1}{m}\sum_{j=-k}^{k} R_{i+j} \quad (3)$$

where R is the original time series, i an index for the time of iteration, j an index for sampling inside the window, and k the number of sampling on one side of the window. The window length $m = 2k+1$. Y is the input time series after one iteration. Different scales of motions are obtained by changing the window length and the number of iterations (Milanchus et al. 1998; Eskridge et al. 1997). The filter periods of less than N days can be calculated with window length m and the number of iteration p, as follows:

$$\mathrm{m} \times p^{\frac{1}{2}} \leq N \quad (4).$$

Therefore, the cycles of 33 days can be removed by a KZ(15, 5) filter with the window length of 15 and 5 iterations. In Equation 5, BL(t) is the O_3 and meteorological time series obtained by KZ(15,5) filter and refers to their baseline variations which are the sum of the long term L(t) and the seasonal component S(t).

$$BL(t) = KZ_{(15,5)} = L(t) + S(t) = KZ_{(183,3)} + S(t) \quad (5).$$

The long-term trend is separated from the raw data obtained by KZ (183, 3) with the periods of > 632 days, and then the seasonal and the short-term component $W(t)$ can be defined as

$$S(t) = KZ_{(15,5)} - KZ_{(183,3)} \quad (6),$$

$$W(t) = \mathrm{X(t)} - \mathrm{BL(t)} = \mathrm{X(t)} - KZ_{(15,5)} \quad (7).$$

After KZ filtering, the meteorological adjustment is conducted by the multivariate regression between the O_3 concentration and meteorological factors such as T, RH, wind speed and sunshine duration (Wise and Comrie 2005; Papanastasiou et al. 2012).

$$A_{BL}(t) = a_{BL} + \sum b_{BLi} \cdot M_{BLi} + \epsilon_{BL}(t) \quad (8),$$

$$A_W(t) = a_W + \sum b_{Wi} \cdot M_{Wi} + \epsilon_W(t) \quad (9),$$

$$\epsilon(\mathrm{t}) = \epsilon_{BL}(t) + \epsilon_W(t) \quad (10),$$

$$A_{ad}(t) = \epsilon(t) + \sum b_{BLi} \cdot \overline{M}_{BLi} + \sum b_{Wi} \cdot \overline{M}_{Wi} + a_{BL} + a_W \quad (11).$$

the multivariate regression models between baseline and short-term O_3 and meteorological factors are shown in Equations 8 and 9. The $A_{BL}(t)$ and M_{BLi} represent the sum of the long term L(t) and the seasonal component S(t) of O_3 concentration and meteorological factors. The $A_W(t)$ and M_{Wi} represent the short-term W(t) of O_3 concentration and meteorological factors. The a and b are the fitted parameters, and i is time point (days). $\epsilon(t)$ is the residual term. The average meteorological condition $\overline{M}$ at the same calendar date during the 5 years is regarded as the base condition for that date, and the meteorological adjustment is conducted against the base condition. In these steps, $A_{ad}(t)$ refers to the meteorologically adjusted O_3 variation with the homogenized annual variation in meteorological conditions. The difference between raw O_3 time series and $A_{ad}(t)$ represents the meteorological impact.

2.4. Classification of SWPs

In order to find the detailed variation characteristics of SWPs, we first extract the predominant SWPs in the warm seasons over the YRD using a weather classification method. Common objective classification methods include using predefined type, the leader algorithm, the cluster analysis, optimization algorithms and eigenvectors (Philipp et al. 2016). The PTT method, a simplified variant of t-mode principal component analysis using orthogonal rotation, is used to classify SWPs during 2014–2018. It is one of the methods for weather classification in European Cooperation in Science and Technology Action 733 (Philipp et al. 2016), which is widely used in atmospheric sciences (Hou et al. 2019).

206 **2.5. FNL and ERA-Interim meteorological data**

207 The National Center for Environmental Prediction Final Operational Global Analysis (FNL)
208 data (http://rda.ucar.edu/datasets/ds083.2/) produced by the Global Data Assimilation System are
209 used in classifying SWPs and analyzing atmospheric circulations. The data have a horizontal
210 resolution of 2.5°×2.5°, with 144×73 horizontal grids available every 6 hours. From the near surface
211 layer to 10 hPa, there are 17 pressure levels in the vertical direction. The data of the geopotential
212 height and wind at 500 hPa and 850 hPa, the vertical wind (W), temperature are used in this study.
213 At the same time, the low cloud cover (LCC), the total cloud liquid water (TCLW) and solar
214 radiation (SR) from ERA-interim are supplemented in this study, which have the same temporal and
215 spatial resolutions as the FNL data. Moreover, the western Pacific Subtropical High index (WPSHI)
216 and the eastern Asian summer monsoon index (EASMI) are calculated using the FNL data of the
217 geopotential height and wind at 850 hPa. The WPSHI is defined following the western Pacific
218 Subtropical High intensity index in the National Climate Center of China. Specific formula refers
219 to website (https://cmdp.ncc-cma.net/extreme/floods.php?product=floods_diag). The EASMI is a
220 shear vorticity index. It is defined as the difference of regional mean zonal wind at 850 hPa between
221 5 and 15°N, 22.5 and 32.5°N, 90 and 130°E, and 110 and 140°E in Wang and Fan (1999),
222 recommended by Wang et al. (2008).

223 The FNL geopotential height field at 850 hPa can capture the synoptic circulation variations
224 over the YRD well (Shu et al. 2017). In this study, we use the geopotential height at 850 hPa from
225 April to September during 2014–2018 as the input for the PTT. WPSHI and EASMI are correlated
226 with the O_3 time series. We used the Pearson correlation coefficient to calculate the correlations
227 between two time series.

228

229 **2.6. Reconstruction of O_3 concentration based on SWP**

230 To quantify the inter-annual variability captured by the variations (frequency and intensity) in
231 the SWPs, Yaranl (1992) provided an algorithm to find the contribution of SWPs frequency variation
232 to the inter-annual O_3 variation. The specific calculation is as follows.

233 $$\overline{\overline{O_{3m}}}(fre) = \sum_{k=1}^{6} \overline{O_{3k}} F_{km} \qquad (12),$$

234 where $\overline{\overline{O_{3m}}}(fre)$ is the reconstructed mean O_3 concentration influenced by the frequency variation

in SWPs from April to September for year m, $\overline{O_{3k}}$ is the 5-year mean O_3 concentration for SWP k, and F_{km} is the occurrence frequency of SWP k during April–September for year m.

Hegarty et al. (2007) suggested that changes in the SWP include both frequency change and intensity change. The intensity of SWPs represents the location and strength of the weather system. Moreover, they noted that the environmental and climate-related contributions to the inter-annual variations of O_3 could be better separated by considering these two changes. So, Equation 12 is modified into the following form.

$$\overline{\overline{O_{3m}}}(fre+int) = \sum_{k=1}^{6}(\overline{O_{3k}} + \Delta O_{3km})F_{km} \quad (13),$$

where $\overline{\overline{O_{3m}}}(fre+int)$ is the reconstructed average O_3 concentration influenced by the frequency and intensity changes of SWPs from April to September for year m; ΔO_{3km} is the modified difference on the fitting line, which is obtained through a linear fitting of the annual O_3 concentration anomalies (ΔO_3) to the SWP intensity index (SWPII) for SWP k in year m. ΔO_{3km} represents the part of the annual observed O_3 oscillation caused by the intensity variation in each SWP. Hegarty et al. (2007) used the domain averaged sea level pressure to represent the circulation intensity index (CII). Liu et al. (2019) reconstructed the inter-annual O_3 level in the northern China using the center pressure of the lowest pressure system. However, we find the intensity variation in each SWP is different when O_3 increases. So we select different SWPII under each SWP according to the characteristics of high O_3 concentration. Lastly, we select the maximum height in zone-1 (25°N–40°N, 110°E–130°E), the maximum height in zone-2 (20°N–50°N, 90°E–140°E) and the mean height in zone-3 (10°N–40°N, 110°E–130°E). Especially, zones1, 2 and 3 were selected in term of location of dominated weather systems under each SWP. Detailed demonstration is introduced in section 3.5.

3. Results and discussion

3.1. Spatio-temporal variations of O_3 in the YRD region

3.1.1. Inter-annual variations of O_3

Fig. 1a shows the time series of the anomalies of the monthly mean O_3 concentration over the YRD from April to September during 2014–2018, as well as the corresponding linear fitting curve. Fig. 1b shows the annual variation in the total number of days with O_3 concentration exceeding the

national standard during the warm seasons over 2014-2018. As shown in Fig. 1a, the monthly mean O_3 concentration in the warm seasons increases over 2014-2018, reaching the maximum of 37.4 ppb in 2017 and maintaining at a high level in 2018. According to the generalized least-squares method with auto-regression in section 2.2, obtained fitting function is $y_t = -0.808 + 0.052t - 0.482\cos\left(\frac{2\pi M}{6}\right) + 0.665\sin\left(\frac{2\pi M}{6}\right) + R_t$. Specifically, 5.2% (1.8 ppb) of k value as the O_3 inter-annual variation shows a large increasing trend in the YRD, which is slightly higher than that in the entire China (5.0% per year, Lu et al. 2020). Meanwhile, the annual average days with O_3 exceeding the standard during the warm seasons also show an increasing trend, reaching a peak in 2017 and maintaining at a high level in 2018. In all, both means and extremes of O_3 concentration have increased over the YRD.

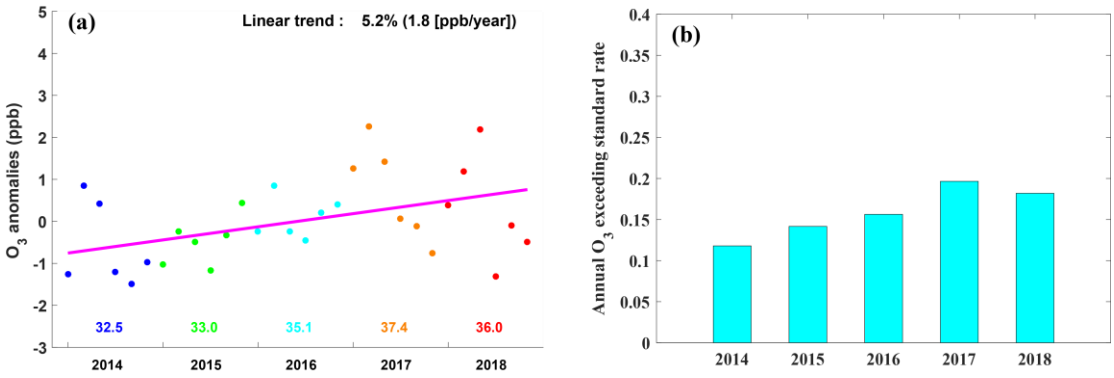

Fig. 1. (a) Anomalies of monthly average O_3 concentration from April to September during 2014–2018. The purple solid line represents the linear fitted curve ($y_t = -0.808 + 0.052t$), and the color number represents the annual (April–September) mean of O_3 concentration. (b) Annual (April–September) variation in the days with O_3 exceeding the national standard.

3.1.2. Characteristics of O_3 variability based on the EOF analysis

To further discuss the spatio-temporal distribution characteristics of the observed O_3 concentration, the EOF approach is used to uncover the relationship between the spatial distribution and temporal variation. By removing the missing data for 17 days, O_3 concentrations in 898 days are processed. The percentages of variance contribution for the first three patterns are 65.7 %, 13.8 % and 9.1 %, respectively. The significance tests of the EOF eigenvalue confirm that the first three patterns are significantly separated. Approximately 88.6 % of the variability in the original data is

contained in these three patterns. In the first EOF pattern (EOF1), the observed O_3 over the YRD changes similarly and the center of the variation is located in the middle of the YRD (Fig. 2a). As shown in Fig. 2b, the time series of EOF1 presents an increasing trend and shows a high negative correlation with the time series of O_3 ($R = 0.98$). Therefore, to some extent, the EOF1 time series variation can represent the daily mean O_3 variation and implies an increasing trend of regional mean O_3 concentration during these periods. Furthermore, we investigated the relationships between the time series of EOF1 and different weather systems, as well as the meteorological factors. Weather systems include the WPSH and the East Asian summer monsoon, which are dominant weather systems affecting the YRD. Both of them show a poor correlation with the EOF1 time series ($R_{WPSHI} = -0.13$ and $R_{EASMI} = -0.04$). It indicates that the daily O_3 variation is too complex to be comprehensively explained through the change in a single weather system. Furthermore, the RH and SR present a good correlation with the EOF1 time series ($R_{RH} = -0.59$ and $R_{SR} = 0.56$). However, it is still unclear how the change in different weather systems causes the variation in RH and SR, and how the variations in RH and SR impact the other meteorological factors and O_3 accumulation.

In the second EOF pattern (EOF2), there is obvious east-west contrast. In contrast, the third EOF (EOF3) pattern presents a notable south-north contrast. At the same time, the increasing trend of EOF2 time series and the decreasing trend of EOF3 time series indicate that O_3 concentrations in the west and northwest have risen from 2014 to 2018. It implies that a higher rate of O_3 increasing would occur in the northwest. As known, the variance contribution of EOF1 is 65.7 % that is greater than EOF2 (13.8 %) and EOF3 (9.1 %). Therefore, increases in O_3 in the entire YRD region is the main trend.

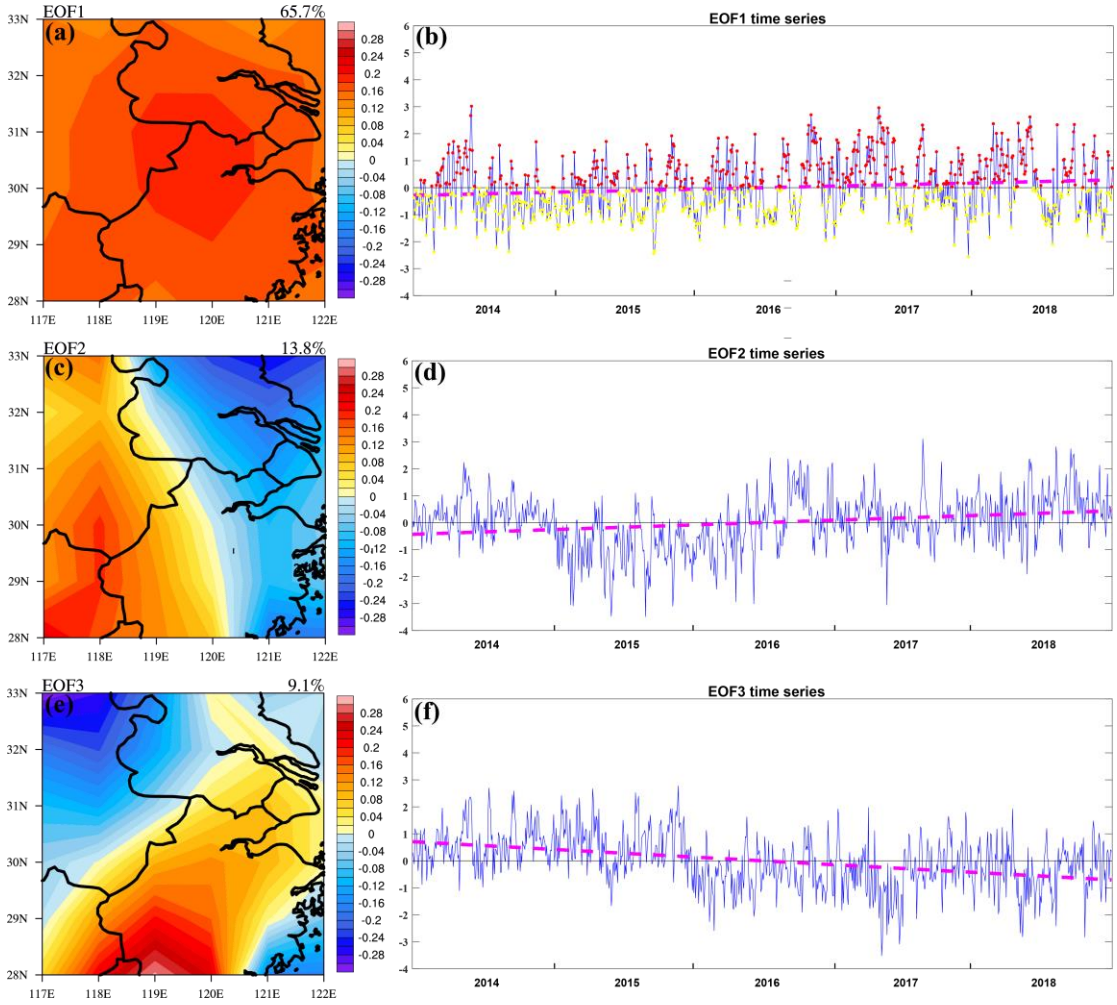

Fig. 2. Three EOF patterns of O_3 concentration in the warm seasons from 2014 to 2018, including the spatial pattern (a, c and e) and time coefficient (b, d and f). The percentage in panels (a, c and e) is the variance contribution of each EOF mode. The pink dash line in panels (b, d and f) represents the linear fitted curve.

3.2. Effects of meteorological conditions on O_3 concentration over the YRD region

3.2.1. Quantifying the effects of meteorological conditions

With the primary pollutant emissions being cut down, the surface O_3 increase in the recent years in China might be attributable to a variety of factors, one of which was suggested to be the slowing down sink of hydroperoxy radicals, related to the variation in $PM_{2.5}$ (Li et al. 2019). Yet, it is uncertain how meteorological conditions influence the increasing trend in surface O_3. Yang et al. (2019) quantified the meteorological impact on O_3 variation over the Pearl River Delta region using the meteorological adjustment. Using the methodology similar to that in Yang et al. (2019), we

investigate meteorological influences on the increase in ozone over the YRD in the warm seasons during 2014–2018. Fig. 3a shows the ambient O_3 variation from 2014 to 2018: i.e. O_3 concentration increases from 2014, reaches the maximum in 2017, and maintains at a relatively high level in 2018. After the meteorological adjustment, the variable magnitude is lower than the original one, implying that if the meteorological conditions remained unchanged over the 5 years, the variation in ambient O_3 concentration would be lower. The meteorological impact can be examined from the difference between the black solid and dashed lines in Fig. 3a. The difference is negative from 2014 to the middle of 2016 and positive from middle of 2016 to 2018. In 2017, the meteorological conditions increase O_3 concentration by about 1.2 ppb. However, in 2015, the meteorological conditions become unfavorable to the O_3 accumulation, leading to an O_3 reduction of 1.4 ppb. The meteorological conditions make a difference in O_3 concentration by 3.1 ppb at most between the most favorable year (2017) and the most unfavorable year (2015), which roughly corresponds to 8.7% ($\frac{max(MEO\ \ imapct)-min(MEO\ \ impact)}{O3(5\ \ year\ \ average)}$) of the annual O_3 concentration.

In addition, we select the most influential meteorological factors to discuss their impacts on O_3 variation, including T2, RH, SR, LCC and WS. As shown in Fig. 3b, RH is the most crucial factor and its variation is similar to the variation in the total meteorological impact. In addition, SR and LCC also play important roles and have large impacts on O_3 variation. RH can impact O_3 concentration in two ways. One is gas phase H_2O reacting with O_3 ($O_3 + H_2O(gas) + hv \rightarrow O_2 + 2OH$). The other is its influencing on clouds and thereby shielding SR. The East Asian summer monsoon plays a key role in affecting the local RH, and meanwhile it might bring a certain amount of O_3 from the areas south of the YRD. However, O_3 concentration is high negatively related to RH, which implies that the local chemical reaction might contribute to the O_3 accumulation more than the regional transport. The impacts of T2 and WS are inconsistent with the overall meteorological impacts.

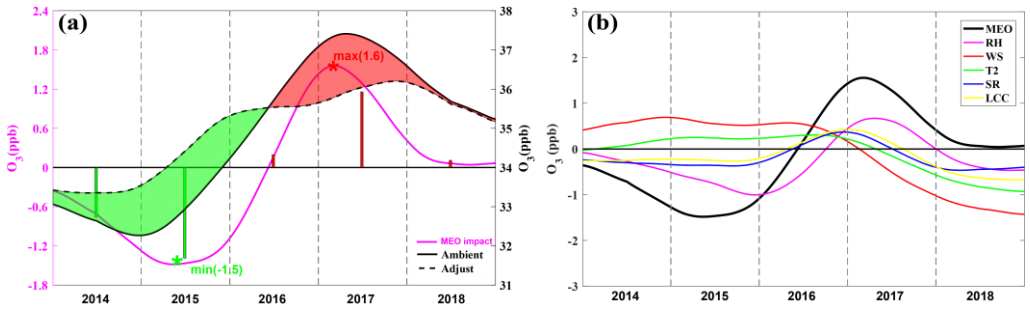

Fig. 3. (a) 5-year trends of ambient O_3 (solid black line), meteorological adjusted O_3 (dashed black line), and the meteorological impact (pink line) over the YRD during 2014–2018. Periods with positive and negative meteorological impacts are shaded in red and green, respectively; red and green bars represent the O_3 increases and decreases attributable to meteorological influences in each year. (b) 5-year variations in the meteorological impact of different meteorological factors (MEO), including relative humidity (RH), solar radiation (SR), air temperature (T2), wind speed (WS) and low cloud cover (LCC).

3.3. Dynamic processes of O_3 variation driven by synoptic circulations

As discussed in section 3.2, the local meteorological factors have a large impact on the O_3 variation. However, to some extent, the variation in local meteorological factors is largely affected by the synoptic-scale weather circulations (Leibensperger et al. 2008; Fiore et al. 2003; Wang et al. 2016). For example, in summer the YRD is under a hot-wet environment controlled by the WPSH. While in winter it is under a cold-dry environment affected by the northwesterly flow caused by the Siberian High. The different weather systems under their corresponding SWPs have their unique meteorological characteristics. Moreover, even under one SWP, the location and intensity changes in a specific weather system can cause the changes in local meteorological factors correspondingly (Gao et al. 2020).

3.3.1. The main synoptic weather patterns in the warm season over the YRD

Applying the PTT classification method, nine SWPs are identified for the warm seasons in the YRD. Due to the relatively large variance, the first dominant five SWPs are selected, and the other four SWPs are grouped as ‘others’. As shown in Table 1, SWP1, SWP2 and SWP4 are dominant, accounting for 41.4%, 23.3% and 14.3% of the occurrence frequency, respectively. In contrast,

SWP3, SWP5 and other types occur in low frequencies, being 7.8%, 7.1% and 6.1%, respectively. Specifically, SWP1 is under control of the southwesterly flow introduced by the WPSH. SWP2 is influenced by the northwesterly flow introduced by a continental high pressure and the Aleutian low pressure. SWP4 is influenced by the southeasterly flow introduced by the WPSH and a cyclone. SWP3 and SWP5 are affected by a cyclone and an anticyclone. SWP1 and SWP4 are with high T2 and RH induced by the southerly flow. While under SWP5, the YRD is with high T2 and low RH because of the northerly flows are weakened and could not carry sufficient water vapor. SWP2 is with relatively low T2. SWP3 is under the control of a cyclone and the strong upward motion, it is with weak SR and low T2. Specific figures of atmospheric circulation at 850 hPa under the five SWPs are provided in the supplement.

TABLE 1. The occurrence days and frequency, typical characteristics, regional mean ± the standard error for T2, RH, WS and SR and positive and negative days under each SWP. The > 0 and > 0.5 represent the value of EOF1 time series more than 0 and 0.5, respectively. The < 0 and < 0.5 is on the contrary.

Type and number of days (frequency)	Typical characteristic of SWPs	Meteorological factors	Pos (>0 and >0.5) Neg (<0 and <0.5) (number of days)
SWP1 372 (41.4%)	Southwesterly flow introduced by WPSH	T2(℃): 28.4 ± 4.9	
		RH (%): 78.0 ± 10.4	175, 112
		WS (m/s): 7.3 ± 0.5	194, 125
		SR (W/m^2): 1606.2 ± 537.8	
SWP2 209 (23.3%)	Northwesterly flow introduced by a continental high pressure and the Aleutian low pressure	T2 (℃): 26.4 ± 5.4	
		RH (%): 74.0 ± 12.9	110, 73
		WS (m/s): 7.3 ± 0.5	97, 57
		SR (W/m^2): 1615.0 ± 563.2	
SWP3 70 (7.8%)	an extratropical cyclone	T2 (℃): 25.4 ± 4.4	
		RH (%): 86.8 ± 6.3	12, 6
		WS (m/s): 7.3 ± 0.6	58, 45

		SR (W/m^2): 959.7 ± 478.1	
SWP4 128 (14.3%)	Southeasterly flow brought by WPSH and a southern cyclone system	T2 (℃): 29.3 ± 4.2 RH (%): 78.7 ± 8.5 WS (m/s): 7.1 ± 0.6 SR (W/m^2): 1506.0 ± 539.0	46, 30 82, 58
SWP5 64 (7.1%)	The north China anticyclone system	T2(℃): 28.1 ± 5.0 RH (%): 74.0 ± 12.0 WS (m/s): 7.2 ± 0.5 SR (W/m^2): 1586.8 ± 479.7	40, 24 23, 14
others 55 (6.1%)	/	/	/

3.3.2. Impacts of SWP change on O_3 concentration variation

We explore the impacts of SWP change on O_3 variation through an analysis combined with EOF. As illustrated in section 3.1.2, the EOF1 mode is the dominant mode, and it implies the increase of O_3 in the entire YRD is the main trend. The EOF1 time series is closely correlated to the regional mean O_3 concentration (R = 0.98). In this study, we primarily focus on why O_3 concentration increases in the entire YRD region, rather than on why the increases in O_3 differ spatially inside the YRD. Therefore, we use the EOF1 time series as a proxy to present the regional O_3 concentration. In Table 1, the positive phase (Pos) represents that the EOF1 time series is more than 0 and it is beneficial to the production and accumulation of O_3. On the contrary, the negative phase (Neg) corresponds low O_3 concentrations. We extract the information by comparing Pos with Neg to find the changes in each SWP. Yin et al. (2019) explored dominant patterns of summer O_3 pollution and associated atmospheric circulation changes in eastern China. Differently from their study, we analyzed the daily variation in SWPs, and thus identified the change in atmospheric circulations more precisely.

In the five main SWPs, the EOF1 time series show an increase trend during their occurrence days in the warm seasons. It means that the five main SWPs tend to bring high ambient O_3 concentration through changes in the SWPs, which include SWP changes in both frequency and

intensity. We find that the change in SWP intensity impacts more significantly the inter-annual variation in O_3 levels than the change in SWP frequency, consistent with the results of Hegarty et al. (2007) and Liu et al. (2019). This will be further discussed in section 3.4. In the following, we will concretely discuss the variation characteristics of the five SWPs and their impacts on the increase of O_3 in the YRD. Especially, we will show atmospheric circulations at 850 hPa and 500 hPa, meteorological factors including SR, T2, LCC, TCLW, RH, meridional wind at 850hPa (V850) and W (vertical velocity) under positive and negative phase of all SWPs, and correlation coefficients of RH, SR and T2 with EOF1 time series under all SWPs.

As shown in previous study, SR, T2 and RH are dominated meteorological factors and can directly impact O_3 photochemical formation and loss (Xie et al. 2017; Gao et al. 2020). To explore the importance and difference of their impacts on O_3 concentrations under different SWPs, we calculate the correlation coefficients between the EOF1 time series and these meteorological factors under each SWP. As shown in table 2 and 3, when the absolute values of the calculated correlation coefficients under a SWP are greater than 0.40, the corresponding meteorological factors present significant changes between Pos and Neg phases. Therefore, we regard them as the crucial meteorological factors that impact O_3 variation under that SWP. In the end, we find that significant decreases in RH and increases in SR are the crucial meteorological factors under SWP1, SWP4 and SWP5. For SWP2, significant decreases in RH, increases in SR and T2 are the crucial meteorological factors. For SWP3, significant decreases in RH is the crucial meteorological factor. Hereinafter, we discuss variations in crucial meteorological factors induced by change in atmospheric circulations.

TABLE 2. Correlation coefficients of RH, SR and T2 with EOF1 time series under each SWP.

Variable	SWP1	SWP2	SWP3	SWP4	SWP5
RH	-0.59	-0.52	-0.50	-0.64	-0.59
SR	0.58	0.56	0.33	0.46	0.48
T2	0.19	0.41	0.26	0.15	0.30

Fig. 4 shows the atmospheric circulations at 850 hPa and 500 hPa, and Table 3 shows meteorological factors including SR, T2, TCC, TCLW, RH, V850 and W for SWP1_Pos and SWP1_Neg. As shown in Figs. 4a and 4b, the YRD is located at the northwest of the WPSH, mainly

affected by the southwesterly winds. Due to the weakening of the WPSH, compared with V850 of 4.3 m/s under SWP1_neg, weakening V850 of 2.9 m/s under SWP1_pos bring a less amount of water vapor to YRD region, therefore, RH significantly decreases by 15.2%. At 500 hPa, a shallow trough located at approximate 113°E is replaced by a slowly straight westerly flow, and the downward motion would strengthen and last longer. Besides, significant decreases in RH under the downward motion condition hinder cloud formation. LCC and TCLW decrease by 0.30 and 0.11, respectively. Furthermore, SR significantly increases by 730.1 W/m^2 due to the less shelter of the clouds and less reflection above the cloud. Eventually, significant decreases in RH and increases in SR lead to stronger O_3 photochemical reaction.

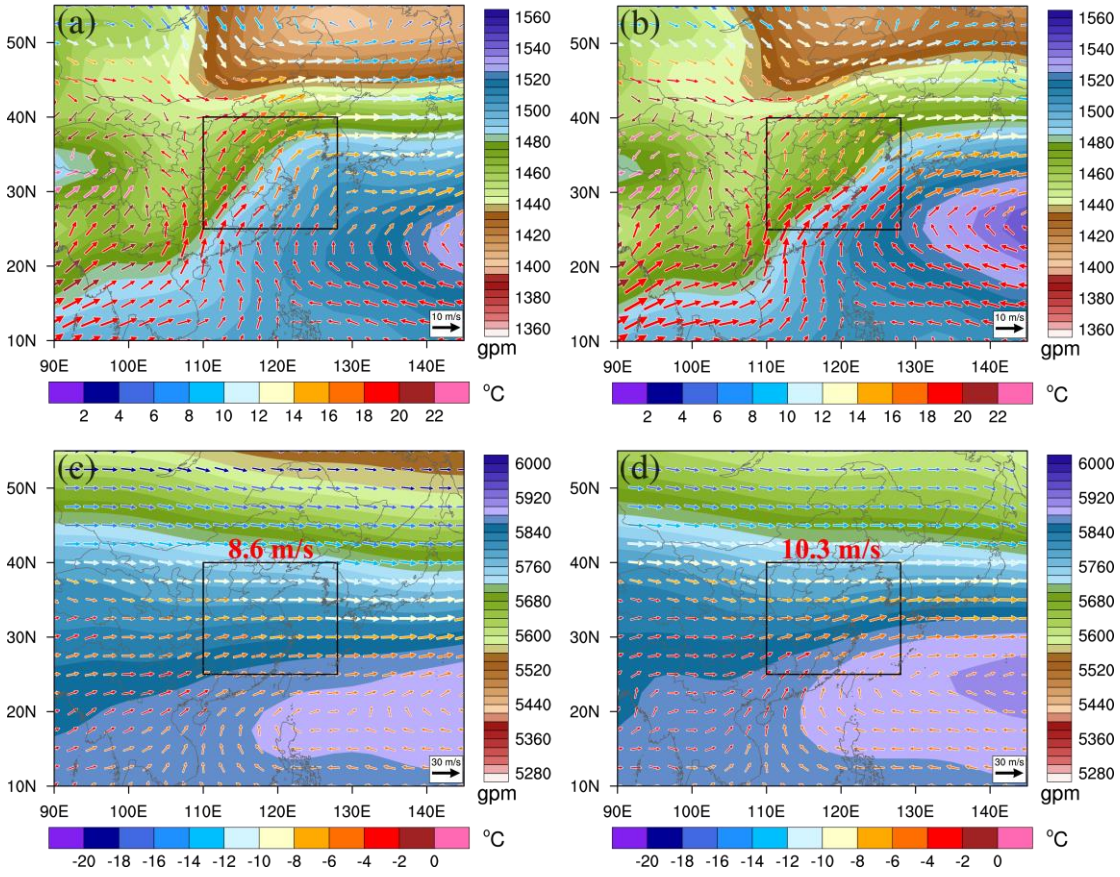

Fig. 4. The geopotential height (shaded) and 850 hPa wind with temperature (color vector) under (a) SWP1_Pos and (b) SWP1_Neg. The geopotential height (shaded) and 500 hPa wind with temperature (color vector) under (c) SWP1_Pos and (d) SWP1_Neg. The red values represent the regionally averaged wind speed at 500 hPa in the zone around black lines. The boxed area in Figs. 4a-d encloses the YRD.

Fig. 5 shows the atmospheric circulations at 850 hPa and 500 hPa, and Table 3 shows meteorological factors including SR, T2, TCC, TCLW, RH, V850 and W for SWP2_Pos and SWP2_Neg. As shown in Figs. 5a and 5b, the YRD is affected by a continental high and the Aleutian low, characterized by northwesterly flow and a bit southwesterly flow. Compared with the SWP2_Neg, the continental high in SWP2_Pos is weakening. Therefore, the YRD region is influenced by warm flows and T2 significantly increases by 4.9 ℃. The correlation between the EOF1 time series and T2 under SWP2 ($R_{T2\text{-}SWP2} = -0.41$) is closer than the correlation in the whole period ($R_{T2\text{-}all} = -0.24$). This implies that the weakening of the continental high plays an important role in enhancing O_3 there. Meanwhile, as the Aleutian low moves southward slightly, the southwesterly flow can hardly bring water vapor to the YRD, which leads to significant decreases in RH by 14.8%. At 500 hPa, a trough located at approximate 120°E–125°E is strengthened associated with Aleutian low shifting southward, leading to the stronger downward motion in the northwestern YRD behind the strengthening trough. Just like SWP1, stronger downward motion and significantly decreasing RH enhance SR significantly by 790.1 W/m^2. Significant decreases in RH, increases in SR and T2 are beneficial to O_3 formation.

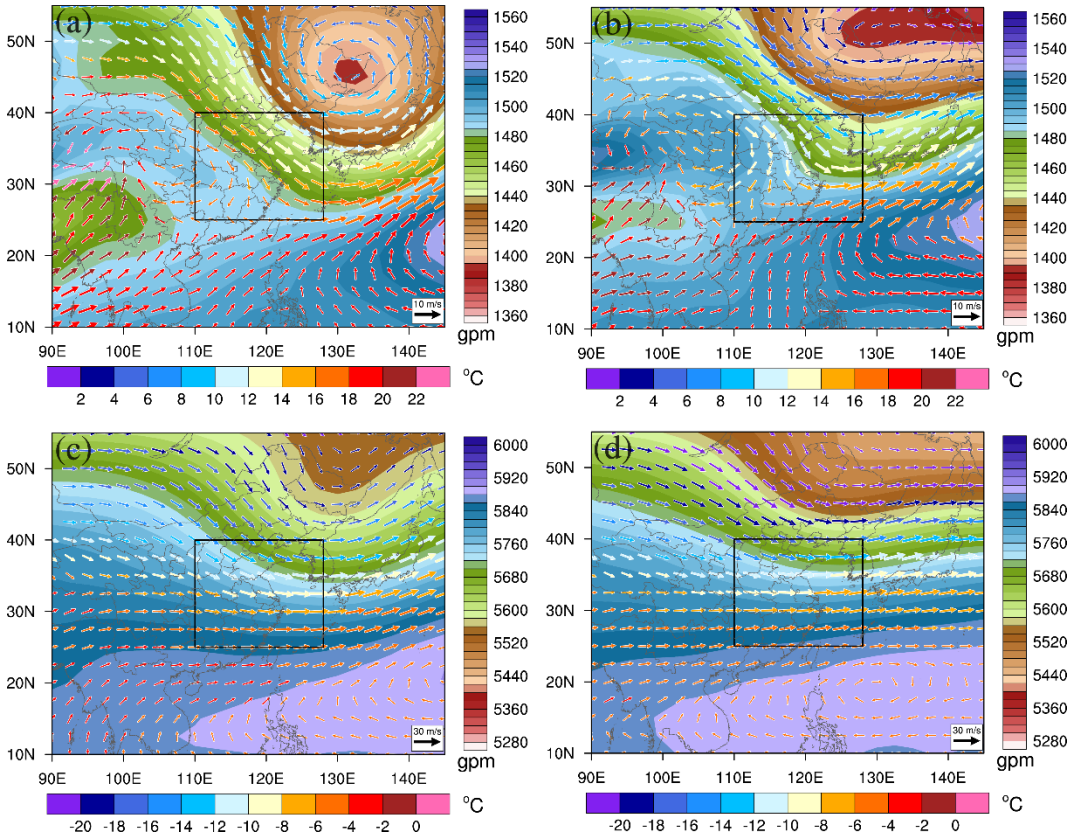

Fig. 5. The geopotential height (shaded) and 850 hPa wind with temperature (color vector) under (a) SWP2_Pos and (b) SWP2_Neg. The geopotential height (shaded) and 500 hPa wind with temperature (color vector) under (c) SWP2_Pos and (d) SWP2_Neg. The boxed area in Figs. 5a-d encloses the YRD.

Fig. 6 shows the atmospheric circulations at 850 hPa and 500 hPa, and Table 3 shows meteorological factors including SR, T2, TCC, TCLW, RH, V850 and W for SWP3_Pos and SWP3_Neg. As shown in Figs. 6a and 6b, the YRD is controlled by an extratropical cyclone. Compared with the SWP3_Neg, the low pressure in SWP3_Pos strengthens and its location is slightly further eastward. Under this circumstance, the weakening southerly flow could hardly bring water vapor to the YRD and thus RH significantly decreases by 11.7%. At 500 hPa, the upward motion would be weakening due to the eastern movement of cyclone and western area controlled by back of a strengthening trough located at about 120°E. However, LCC still is at a high level under upward motion condition. Furthermore, high LCC and its less variation lead to low SR. Therefore, the correlation coefficient between SR and EOF1 time series is relatively low under this

SWP3 ($R_{SR\text{-}SWP3}$=-0.33). Lastly, only significant decreases in RH would be crucial factor for high O_3 concentration.

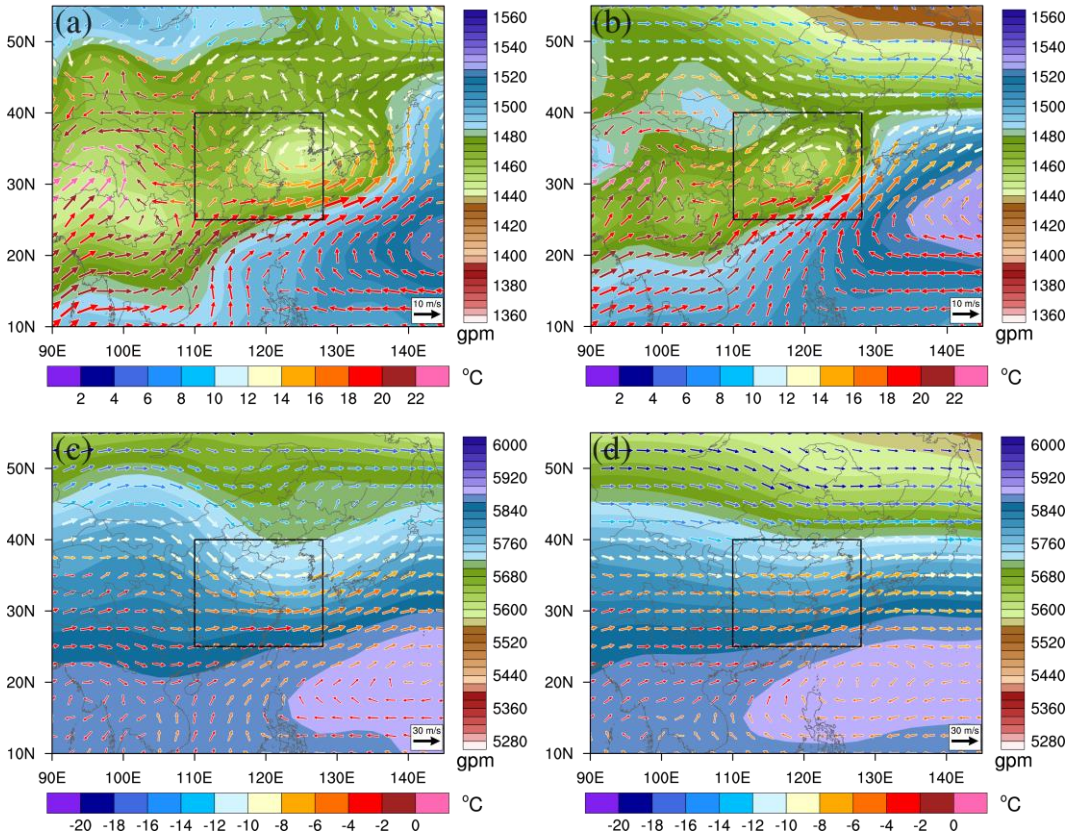

Fig. 6. The geopotential height (shaded) and 850 hPa wind with temperature (color vector) under (a) SWP3_Pos and (b) SWP3_Neg. The geopotential height (shaded) and 500 hPa wind with temperature (color vector) under (c) SWP3_Pos and (d) SWP3_Neg. The boxed area in Figs. 6a-d encloses the YRD.

Fig. 7 shows the atmospheric circulations at 850 hPa and 500 hPa, and Table 3 shows meteorological factors including SR, T2, LCC, TCLW, RH, V850 and W for SWP4_Pos and SWP4_Neg. As shown in Figs. 7a and 7b, southeasterly winds prevail in the YRD, which is modulated by a southern low pressure and WPSH. Compared with the SWP4_Neg, the southern low pressure and southeasterly flow in SWP4_Pos is weaker, and thus it brings less water vapor to the YRD and significantly decreases RH by 12.3%. At 500 hPa, a shallow trough located at about 125°E strengthens associated with weakening of the southern cyclone pressure, causing the strong sink motion, less LCC and significant increases in SR by 538.5 W/m^2. Significant increases in SR

and decreases in RH are important for O_3 pollution.

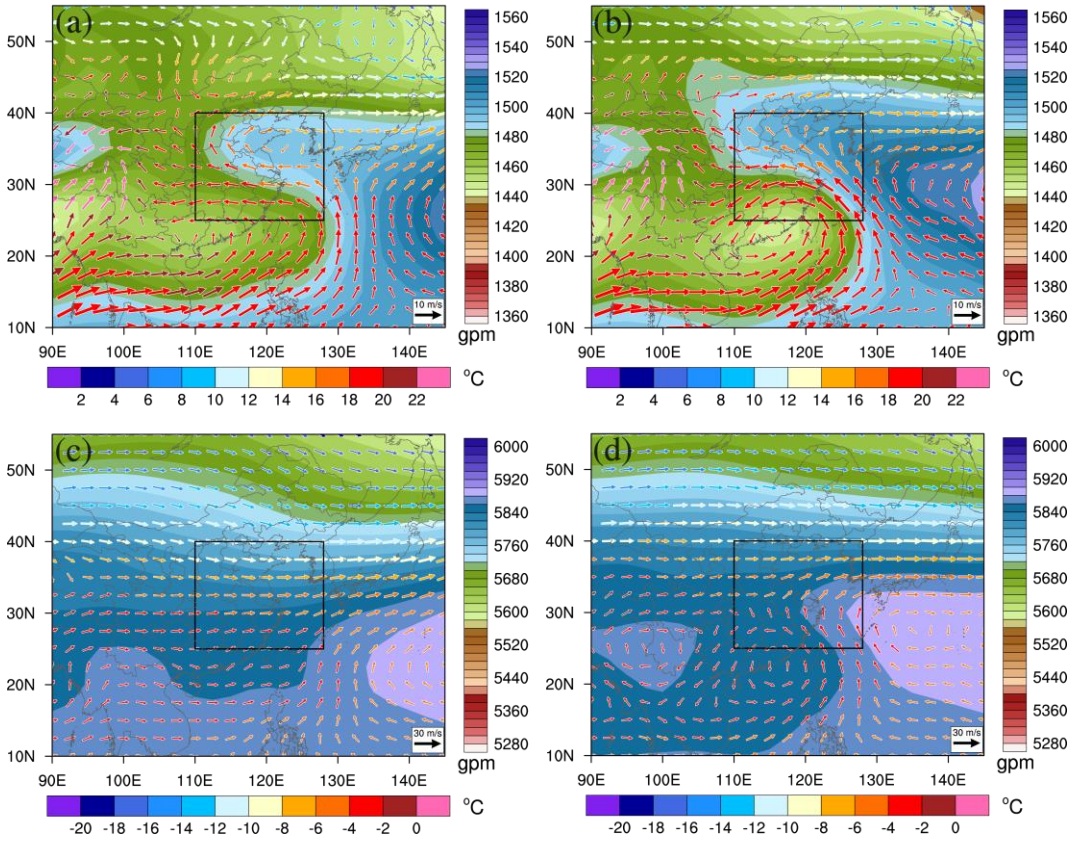

Fig. 7. The geopotential height (shaded) and 850 hPa wind with temperature (color vector) under (a) SWP4_Pos and (b) SWP4_Neg. The geopotential height (shaded) and 500 hPa wind with temperature (color vector) under (c) SWP4_Pos and (d) SWP4_Neg. The boxed area in Figs. 7a-d encloses the YRD.

Fig. 8 shows the atmospheric circulations at 850 hPa and 500 hPa, and Table 3 shows meteorological factors including SR, T2, LCC, TCLW, RH, V850 and W for SWP5_Pos and SWP5_Neg. As shown in Figs. 8a and 8b, the YRD is controlled by the north China anticyclone, characterized by the northeasterly and the southwesterly winds. Compared with the SWP5_Neg, the high pressure in the SWP5_Pos is weaker and the northeasterly flow respond accordingly. The weakened sea flow makes air dryer and RH significantly lower by 17.3%. At 500hPa, a trough located at about 130°E controlling the YRD strengthens associated the Japan low pressure appearance. The downward motions become strong correspondingly and result in significant increases in SR by 628.3 W/m^2. Significant increases in SR and decreases in RH lead to increases

in O_3 concentration.

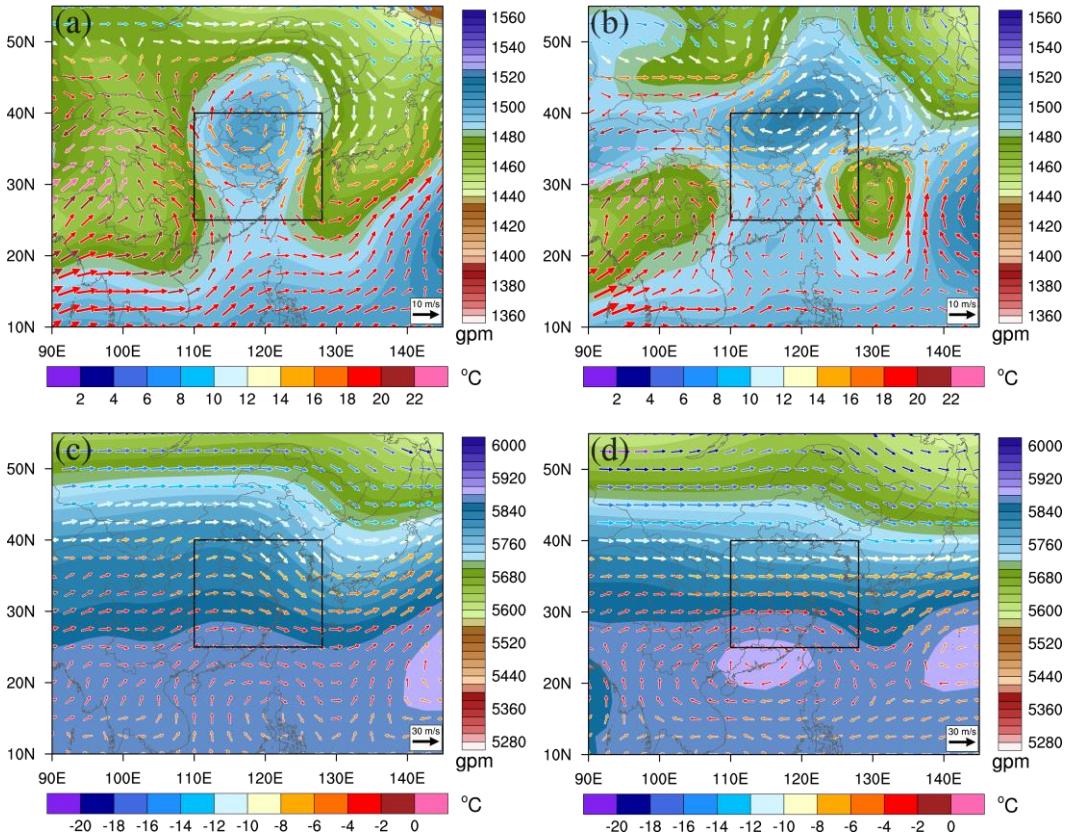

Fig. 8. The geopotential height (shaded) and 850 hPa wind with temperature (color vector) under (a) SWP5_Pos and (b) SWP5_Neg. The geopotential height (shaded) and 500 hPa wind with temperature (color vector) under (c) SWP5_Pos and (d) SWP5_Neg. The boxed area in Figs.8a-d encloses the YRD.

TABLE 3. Regional mean ± the standard error of meteorological factors in Pos and Neg phases and their difference under each SWP pattern.

SWP	phase	RH (%)	SR (W/m^2)	T2 (℃)	LCC	TCLW	V850 (m/s)	W (Pa/s)
P1	Pos	69.7±9.7	1971.0±403.2	29.9±4.8	0.07±0.15	0.06±0.08	2.9±2.2	0.00±0.05
	Neg	84.9±6.5	1240.9±460.2	27.5±4.8	0.37±0.27	0.17±0.14	4.3±2.7	-0.05±0.05
	Diff	-15.2	730.1	2.4	-0.30	-0.11	-1.4	0.05
P2	Pos	66.5±11.0	1968.4±377.1	28.8±4.3	0.07±0.14	0.06±0.09	-2.5±3.1	0.02±0.05
	Neg	81.3±10.8	1178.3±479.6	23.9±5.9	0.48±0.31	0.19±0.14	-1.4±3.2	-0.03±0.06
	Diff	-14.8	790.1	4.9	-0.41	-0.13	-1.1	0.05
P3	Pos	76.9±7.1	1371.4±605.8	27.8±2.5	0.34±0.18	0.21±0.19	-0.7±3.4	-0.02±0.04
	Neg	88.6±5.1	855.0±395.1	24.8±4.6	0.58±0.24	0.31±0.16	1.9±3.7	-0.09±0.06

	Diff	-11.7	516.4	3.0	-0.24	-0.10	-2.6	0.07
	Pos	71.1±7.2	1882.3±388.1	30.6±3.7	0.11±0.16	0.12±0.16	0.6±2.4	0.01±0.04
P4	Neg	83.4±6.8	1343.8±547.5	28.9±4.2	0.35±0.24	0.19±0.19	2.5±3.6	-0.04±0.06
	Diff	-12.3	538.5	1.7	-0.24	-0.07	-1.9	0.05
	Pos	68.5±14.2	1827.5±447.4	29.6±5.3	0.07±0.11	0.09±0.14	-1.8±3.4	0.01±0.04
P5	Neg	85.8±3.5	1199.2±397.2	26.4±3.8	0.43±0.30	0.16±0.09	-2.3±5.3	-0.02±0.04
	Diff	-17.3	628.3	3.2	-0.35	-0.07	0.5	0.03
Others		/	/		/		/	/

3.4. Indicators for reconstructing inter-annual O_3 variation affected by synoptic-scale atmospheric circulation

Due to the similar variations in regional mean O_3 concentration and EOF1 time series, we have reconstructed the inter-annual EOF1 time series to replace the regional mean O_3 concentration by accounting either frequency-variation-only or both frequency and intensity variations in SWPs, which are EOF1 time series (Fre) and EOF1 time series (Fre + Int), respectively. The observed and reconstructed inter-annual EOF1 time series in 2014–2018 over the entire YRD region are shown in Fig. 9. Obviously, the frequency changes in SWPs almost have no impact on the O_3 variability in the entire YRD. However, considering intensity change, the fitting curve would be closer to the EOF1 time series. To obtain the accurate frequency and intensity change contributions, quantitative evaluation is carried out, we define the contribution index as the difference between the maximum and the minimum of a certain reconstructed time series divided by the difference between the maximum and the minimum of inter-annual EOF1 time series: Contribution Index = (The reconstructed maximum – the reconstructed minimum)/(the original maximum – the original minimum). Through the above equation, we derive the relative contribution (contribution index) of the frequency change and the intensity change. Compared with the contribution index of 10.9% for SWPs frequency change, the value of 48.9% for SWPs intensity change accounts for a larger proportion. Therefore, the intensity change in SWP is more important to the inter-annual O_3 variation than the frequency change.

During the reconstructed process, we drastically found that SWPIIs (SWP intensity indexes) definition play an important role to reconstructing curve. In previous studies, Hegarty et al. (2007) and Liu et al. (2019) reconstructed the inter-annual O_3 level in the northeastern United States and the northern China using the same method as ours. They defined the intensity change in SWPs using

551 the domain-averaged sea level pressure and the pressure of the lowest-pressure system. However,
552 the correlation under Hegarty's Pattern V is poor, which has negative effect on their reconstructed
553 curve. Therefore, we select six SWPIIs and judge their rationality through their correlation
554 coefficients with EOF1 time series under each SWP: the maximum geopotential height in zone 1
555 (25°N–40°N, 110°E–130°E) and zone 2 (20°N–50°N, 90°E–140°E), the minimum geopotential
556 height in zone 1 (25°N–40°N, 110°E–130°E) and zone 2 (20°N–50°N, 90°E–140°E), and the
557 average geopotential height in zone 1 (25°N–40°N, 110°E–130°E) and zone 3 (10°N –40°N, 110°E–
558 130°E). As shown in Table 4, for SWP3 and SWP5, the SWPII for the maximum geopotential height
559 in zone 1 has a relative high correlation. For SWP1 and SWP4, the SWPII for the maximum
560 geopotential height in zone 2 has a relative high correlation. We found that the maximum
561 geopotential height show a relatively close correlation with the annual EOF1 time series. It is
562 because the maximum geopotential height reflects the wind speed affecting water vapor transport
563 under this pattern. Compared with SWP3 and SWP5, the weather systems are larger than the
564 classification region for SWP1 and SWP4. So it shows better correlation coefficients in the large
565 zone 2 than in zone 1 under SWP1 and SWP4. For SWP2, when O_3 concentration tends to be at a
566 high level, a cold continental high behind the YRD tends to weaken. Therefore, we select the average
567 geopotential height in zone 3 to represent the SWPII. Table 4 shows that the reconstructed curve
568 becomes good when we select different SWPIIs according to the characteristics of high O_3 level
569 under each SWP.
570

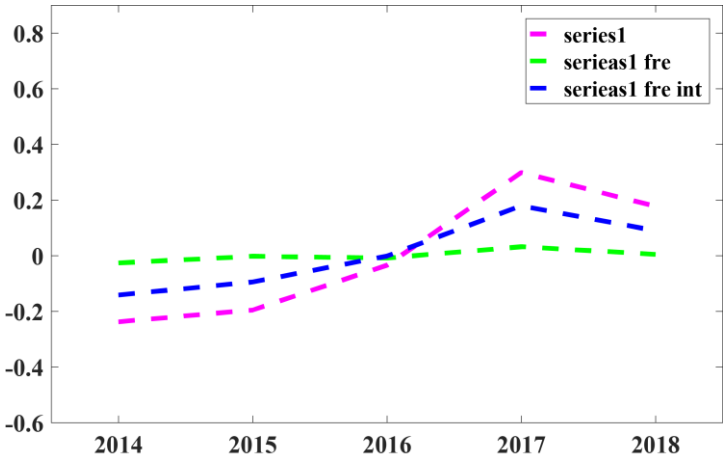

571
572 **Fig. 9. The trend of the inter-annual EOF1 time series in the warm seasons. The pink curve**
573 **represents the original inter-annual EOF1 time series in the warm seasons, the green line**

represents the reconstructed EOF1 time series only accounting the frequency variation in SWPs, and blue line represents the reconstructed one accounting both the frequency and the intensity variations in SWPs.

TABLE 4. Correlation coefficients between EOF1 time series and different SWPIIs under each SWP.

Type	$Z_{1\text{-ave}}$	$Z_{1\text{-max}}$	$Z_{1\text{-min}}$	$Z_{2\text{-min}}$	$Z_{2\text{-max}}$	$Z_{3\text{-ave}}$
SWP1	-0.47	-0.29	-0.35	-0.33	-0.60	-0.32
SWP2	-0.14	-0.08	0.02	-0.07	-0.09	-0.40
SWP3	0.28	0.61	0.03	0.05	0.43	-0.60
SWP4	-0.14	-0.03	-0.17	-0.22	0.78	-0.38
SWP5	0.52	0.76	0.39	0.56	0.72	0.58

4. Conclusions and discussions

In this study, we discussed meteorological influences on the O_3 variation in the warm seasons during 2014–2018 in the YRD, China. Specifically, we analyzed the O_3 spatio-temporal distribution characteristics, quantified the contribution of meteorological conditions to the O_3 variations, explored how changes in SWPs and corresponding meteorological factors lead to O_3 increase in the YRD over 2014–2018, and assessed the contributions of SWP frequency and intensity to the inter-annual O_3 variation in the region. The main conclusions are as follows.

The annual mean O_3 concentrations during the warm seasons averaged over the YRD are 32.5, 33.0, 35.1, 37.4 and 36.0 ppb, respectively, for each year from 2014 to 2018, with a significantly increasing rate of 1.8 ppb $year^{-1}$ (5.2% $year^{-1}$). Meanwhile, the total number of days on which O_3 concentration exceeding the national standard also increases with year in a similar pattern. Through the EOF analysis of O_3 in space and time, three dominant modes were identified. The first mode is the most dominant mode, accounting for 65.7% of the O_3 variation, suggesting that increase tendencies in O_3 prevail over the entire YRD.

We quantified the influence of meteorology on the inter-annual variation and trend of O_3 over the YRD from 2014–2018, and found that the influence could lead to a regional O_3 increase by 3.1

ppb at most. Especially, RH plays the most important role in modulating the inter-annual O_3 variation, followed by SR and LCC. RH impacts on O_3 concentration through two ways. One is gas phase H_2O reacting with O_3 ($O_3 + H_2O(gas) + hv \rightarrow O_2 + 2OH$). The other is its influencing on clouds and thereby shielding SR. To explore connections between the O_3 variation and synoptic circulations, we further identified nine types of SWPs objectively based on the PTT method, and selected five main types to explore their impact on O_3 variation. The typical weather systems of the five SWPs include the WPSH under SWP1, a continental high and the Aleutian low under SWP2, an extratropical cyclone under SWP3, a southern low pressure and the WPSH under SWP4 and the north China anticyclone under SWP5. Combining EOF1 time series variation under each SWP, we found that the variation in all SWPs over 2014–2018 are favorable to O_3 increase during that period. However, the crucial changes in meteorological factors attributable to the increases in O_3 concentrations are different under each SWP. For SWPs 1, 4 and 5, the crucial changes in meteorological factors include significant decreases in RH and increases in SR, which are predominantly attributable to the WPSH weakening under SWP1, the southern low pressure weakening under SWP4, and the north China anticyclone weakening under SWP5. These changes in weather systems prevent the water vapor from being transported to the YRD and result in RH significantly decreased by 15.2, 12.3 and 17.3%, respectively. Moreover, the significant decreases in RH and increases in downward motion (behind the strengthening trough and in front of the strengthening ridge) lead to less LCC, and thereby SR significantly increases by 730.1, 538.5 and 628.3 W/m^2, respectively. Under SWP2, the crucial changes in meteorological factors are significant decrease in RH by 14.8%, and increases in SR by 790.1 W/m^2 and T2 by 4.9 ℃. Significant decrease in RH and increases in SR are mainly induced by the Aleutian low southward extending, which has a similar influential mechanism between RH, LCC and SR with SWPs 1, 4 and 5. In addition, significantly increases in T2 would be due to weakening cold flow introduced by a weakening continental high. Under SWP3, the significant decreases in RH by 11.7% is mainly induced by an intensified extratropical cyclone that blocks the southerly flow carrying water vapor into the YRD. All changes are critical to O_3 formation under each SWP.

As the overall change in SWP intensity and that in SWP frequency contribute to 48.9% and 10.9% to the changes in O_3, we conclude that the change in SWP intensity is more important to the

O_3 increase over 2014–2018 than that in SWP frequency. We further reconstructed the EOF1 time series by considering different SWPIIs due to the unique characteristics of each SWP. The results are better than those in Hegarty et al. (2007) and Liu et al. (2019) who used the same SWPIIs in all SWPs.

This study quantified the inter-annual variation and increasing rate of O_3 in the YRD, China, and explored the connection between SWP variations and the O_3 increase. It provides an enhanced understanding of response of O_3 variation to changes in SWPs from year to year and thus this understanding may be insightful to planning strategies for O_3 pollution control.

Authorship contribution statement

Da Gao: Conceptualization, Data curation, Formal analysis, Meteorology, Investigation, software, Writing – original draft, Writing – revision. **Min Xie**: Conceptualization, Methodology, Writing – revision, Project administration, Funding acquisition. **Jane Liu:** Formal analysis, Meteorology, Writing – revision. **Tijian Wang**: Formal analysis, Funding acquisition. **Chaoqun Ma**: Formal analysis, Meteorology. **Haokun Bai**: Formal analysis, Meteorology. **Xing Chen**: Formal analysis. **Mengmeng Li**: Formal analysis. **Bingliang Zhuang**: Formal analysis. **Shu Li**: Formal analysis

Declaration of competing interest

The authors declare that they have no known competing financial interests or personal relationships that could have appeared to influence the work reported in this paper.

Acknowledgements

This work was supported by the National Key Research and Development Program of China (2018YFC0213502, 2018YFC1506404).

References

Barnes, E. A., and Fiore, A. M.: Surface ozone variability and the jet position: Implications for projecting future air quality, Geophys Res Lett, 40, 2839-2844, 10.1002/grl.50411, 2013.

Cooper, O. R., Schultz, M. G., Schroder, S., Chang, K. L., Gaudel, A., Benitez, G. C., Cuevas, E., Frohlich, M., Galbally, I. E., Molloy, S., Kubistin, D., Lu, X., McClure-Begley, A., Nedelec, P., O'Brien, J., Oltmans, S. J.,

Petropavlovskikh, I., Ries, L., Senik, I., Sjoberg, K., Solberg, S., Spain, G. T., Spangl, W., Steinbacher, M., Tarasick, D., Thouret, V., and Xu, X. B.: Multi-decadal surface ozone trends at globally distributed remote locations, Elementa-Sci Anthrop, 8, Artn 23 10.1525/Elementa.420, 2020.

Day, D. B., Xiang, J., and Mo, J.: Association of ozone exposure with cardiorespiratory pathophysiologic mechanisms in healthy adults (vol 177, pg 1344, 2017), Jama Intern Med, 177, 1400-1400, 10.1001/jamainternmed.2017.4605, 2017.

Doherty, R. M., Wild, O., Shindell, D. T., Zeng, G., MacKenzie, I. A., Collins, W. J., Fiore, A. M., Stevenson, D. S., Dentener, F. J., Schultz, M. G., Hess, P., Derwent, R. G., and Keating, T. J.: Impacts of climate change on surface ozone and intercontinental ozone pollution: A multi-model study, J Geophys Res-Atmos, 118, 3744-3763, 10.1002/jgrd.50266, 2013.

Eskridge, R. E., Ku, J. Y., Rao, S. T., Porter, P. S., and Zurbenko, I. G.: Separating different scales of motion in time series of meteorological variables, B Am Meteorol Soc, 78, 1473-1483, Doi 10.1175/1520-0477(1997)078<1473:Sdsomi>2.0.Co;2, 1997.

Fiore, A. M., Jacob, D. J., Mathur, R., and Martin, R. V.: Application of empirical orthogonal functions to evaluate ozone simulations with regional and global models, J Geophys Res-Atmos, 108, Artn 4431 10.1029/2002jd003151, 2003.

Gao, D., Xie, M., Chen, X., Wang, T. J., Liu, J., Xu, Q., Mu, X. Y., Chen, F., Li, S., Zhuang, B. L., Li, M. M., Zhao, M., and Ren, J. Y.: Systematic classification of circulation patterns and integrated analysis of their effects on different ozone pollution levels in the Yangtze River Delta Region, China, Atmos Environ, https://doi.org/10.1016/j.atmosenv.2020.117760 2020.

Gao, W., Tie, X. X., Xu, J. M., Huang, R. J., Mao, X. Q., Zhou, G. Q., and Chang, L. Y.: Long-term trend of O_3 in a mega City (Shanghai), China: Characteristics, causes, and interactions with precursors, Sci Total Environ, 603, 425-433, 10.1016/j.scitotenv.2017.06.099, 2017.

Han, H., Liu, J. E., Shu, L., Wang, T. J., and Yuan, H. L.: Local and synoptic meteorological influences on daily variability in summertime surface ozone in eastern China, Atmos Chem Phys, 20, 203-222, 10.5194/acp-20-203-2020, 2020.

He, J. J., Gong, S. L., Yu, Y., Yu, L. J., Wu, L., Mao, H. J., Song, C. B., Zhao, S. P., Liu, H. L., Li, X. Y., and Li, R. P.: Air pollution characteristics and their relation to meteorological conditions during 2014-2015 in major Chinese cities, Environ Pollut, 223, 484-496, 10.1016/j.envpol.2017.01.050, 2017.

Hegarty, J., Mao, H., and Talbot, R.: Synoptic controls on summertime surface ozone in the northeastern United States, J Geophys Res-Atmos, 112, Artn D14306 10.1029/2006jd008170, 2007.

Hou, X. W., Zhu, B., Kumar, K. R., and Lu, W.: Inter-annual variability in fine particulate matter pollution over China during 2013-2018: Role of meteorology, Atmos Environ, 214, ARTN 116842 10.1016/j.atmosenv.2019.116842, 2019.

Jacob, D. J., and Winner, D. A.: Effect of climate change on air quality, Atmos Environ, 43, 51-63, 10.1016/j.atmosenv.2008.09.051, 2009.

Jacob, D. J., and Winner, D. A.: Effect of climate change on air quality, Atmos Environ, 43, 51-63, 2009.

Jerrett, M., Burnett, R. T., Pope, C. A., Ito, K., Thurston, G., Krewski, D., Shi, Y. L., Calle, E., and Thun, M.: Long-Term Ozone Exposure and Mortality., New Engl J Med, 360, 1085-1095, Doi 10.1056/Nejmoa0803894, 2009.

Leibensperger, E. M., Mickley, L. J., and Jacob, D. J.: Sensitivity of US air quality to mid-latitude cyclone frequency and implications of 1980-2006 climate change, Atmos Chem Phys, 8, 7075-7086, DOI 10.5194/acp-8-7075-2008, 2008.

Li, K., Jacob, D. J., Liao, H., Shen, L., Zhang, Q., and Bates, K. H.: Anthropogenic drivers of 2013-2017 trends

in summer surface ozone in China, P Natl Acad Sci USA, 116, 422-427, 2019.
Liu, J. D., Wang, L. L., Li, M. G., Liao, Z. H., Sun, Y., Song, T., Gao, W. K., Wang, Y. H., Li, Y., Ji, D. S., Hu, B., Kerminen, V. M., Wang, Y. S., and Kulmala, M.: Quantifying the impact of synoptic circulation patterns on ozone variability in northern China from April to October 2013-2017, Atmos Chem Phys, 19, 14477-14492, 10.5194/acp-19-14477-2019, 2019.
Lu, X., Hong, J. Y., Zhang, L., Cooper, O. R., Schultz, M. G., Xu, X. B., Wang, T., Gao, M., Zhao, Y. H., and Zhang, Y. H.: Severe Surface Ozone Pollution in China: A Global Perspective, Environ Sci Tech Let, 5, 487-494, 10.1021/acs.estlett.8b00366, 2018.
Lu, X., Zhang, L., Chen, Y. F., Zhou, M., Zheng, B., Li, K., Liu, Y. M., Lin, J. T., Fu, T. M., and Zhang, Q.: Exploring 2016-2017 surface ozone pollution over China: source contributions and meteorological influences, Atmos Chem Phys, 19, 8339-8361, 10.5194/acp-19-8339-2019, 2019.
Lu, X., Zhang, L., Wang, X. L., Gao, M., Li, K., Zhang, Y. Z., Yue, X., and Zhang, Y. H.: Rapid Increases in Warm-Season Surface Ozone and Resulting Health Impact in China Since 2013, Environ Sci Tech Let, 7, 240-247, 10.1021/acs.estlett.0c00171, 2020.
Milanchus, M. L., Rao, S. T., and Zurbenko, I. G.: Evaluating the effectiveness of ozone management efforts in the presence of meteorological variability, J Air Waste Manage, 48, 201-215, Doi 10.1080/10473289.1998.10463673, 1998.
Papanastasiou, D. K., Melas, D., Bartzanas, T., and Kittas, C.: Estimation of Ozone Trend in Central Greece, Based on Meteorologically Adjusted Time Series, Environ Model Assess, 17, 353-361, 10.1007/s10666-011-9299-6, 2012.
Philipp, A., Beck, C., Huth, R., and Jacobeit, J.: Development and comparison of circulation type classifications using the COST 733 dataset and software, Int J Climatol, 36, 2673-2691, 10.1002/joc.3920, 2016.
Pu, X., Wang, T. J., Huang, X., Melas, D., Zanis, P., Papanastasiou, D. K., and Poupkou, A.: Enhanced surface ozone during the heat wave of 2013 in Yangtze River Delta region, China, Sci Total Environ, 603, 807-816, 10.1016/j.scitotenv.2017.03.056, 2017.
Rao, S. T., and Zurbenko, I. G.: Detecting And Tracking Changes In Ozone Air-Quality, J Air Waste Manage, 44, 1089-1092, Doi 10.1080/10473289.1994.10467303, 1994.
Rao, S. T., and Zurbenko, I. G.: Detecting And Tracking Changes In Ozone Air-Quality, J Air Waste Manage, 44, 1089-1092, Doi 10.1080/10473289.1994.10467303, 1994.
Santurtun, A., Gonzalez-Hidalgo, J. C., Sanchez-Lorenzo, A., and Zarrabeitia, M. T.: Surface ozone concentration trends and its relationship with weather types in Spain (2001-2010), Atmos Environ, 101, 10-22, 10.1016/j.atmosenv.2014.11.005, 2015.
Shu, L., Xie, M., Wang, T. J., Gao, D., Chen, P. L., Han, Y., Li, S., Zhuang, B. L., and Li, M. M.: Integrated studies of a regional ozone pollution synthetically affected by subtropical high and typhoon system in the Yangtze River Delta region, China, Atmos Chem Phys, 16, 15801-15819, 10.5194/acp-16-15801-2016, 2016.
Shu, L., Xie, M., Gao, D., Wang, T. J., Fang, D. X., Liu, Q., Huang, A. N., and Peng, L. W.: Regional severe particle pollution and its association with synoptic weather patterns in the Yangtze River Delta region, China, Atmos Chem Phys, 17, 12871-12891, 10.5194/acp-17-12871-2017, 2017.
Shu, L., Wang, T., Han, H., Xie, M., Chen, P., Li, M., and Wu, H.: Summertime ozone pollution in the Yangtze River Delta of eastern China during 2013–
2017: Synoptic impacts and source apportionment, Environ. Pollut., 257, 113631, https://doi.org/10.1016/j.envpol.2019.113631, 2020.

745 Wang, B., and Fan, Z.: Choice of south Asian summer monsoon indices, B Am Meteorol Soc, 80, 629-638,
746 Doi 10.1175/1520-0477(1999)080<0629:Cosasm>2.0.Co;2, 1999.
747 Wang, B., Wu, Z. W., Li, J. P., Liu, J., Chang, C. P., Ding, Y. H., and Wu, G. X.: How to measure the strength of
748 the East Asian summer monsoon, J Climate, 21, 4449-4463, 10.1175/2008JCLI2183.1, 2008.
749 Wang, T., Xue, L. K., Brimblecombe, P., Lam, Y. F., Li, L., and Zhang, L.: Ozone pollution in China: A review of
750 concentrations, meteorological influences, chemical precursors, and effects, Sci Total Environ, 575, 1582-
751 1596, 10.1016/j.scitotenv.2016.10.081, 2017.
752 Wise, E. K., and Comrie, A. C.: Extending the Kolmogorov-Zurbenko filter: Application to ozone, particulate
753 matter, and meteorological trends, J Air Waste Manage, 55, 1208-1216, Doi
754 10.1080/10473289.2005.10464718, 2005.
755 Xie, M., Zhu, K. G., Wang, T. J., Yang, H. M., Zhuang, B. L., Li, S., Li, M. G., Zhu, X. S., and Ouyang, Y.: Application
756 of photochemical indicators to evaluate ozone nonlinear chemistry and pollution control
757 countermeasure in China, Atmos Environ, 99, 466-473, 10.1016/j.atmosenv.2014.10.013, 2014.
758 Xie, M., Liao, J., Wang, T., Zhu, K., Zhuang, B., Han, Y., Li, M., and Li, S.: Modeling of the anthropogenic heat
759 flux and its effect on regional meteorology and air quality over the Yangtze River Delta region, China,
760 Atmospheric Chemistry and Physics, 16, 6071-6089, 10.5194/acp-16-6071-2016, 2016a.
761 Xie, M., Zhu, K., Wang, T., Chen, P., Han, Y., Li, S., Zhuang, B., and Shu, L.: Temporal characterization and
762 regional contribution to O3 and NOx at an urban and a suburban site in Nanjing, China, The Science of
763 the total environment, 551-552, 533-545, 10.1016/j.scitotenv.2016.02.047, 2016b.
764 Xie, M., Shu, L., Wang, T.-j., Liu, Q., Gao, D., Li, S., Zhuang, B.-l., Han, Y., Li, M.-m., and Chen, P.-l.: Natural
765 emissions under future climate condition and their effects on surface ozone in the Yangtze River Delta
766 region, China, Atmospheric Environment, 150, 162-180, 10.1016/j.atmosenv.2016.11.053, 2017.
767 Yang, Y., Liao, H., and Li, J.: Impacts of the East Asian summer monsoon on interannual variations of
768 summertime surface-layer ozone concentrations over China, Atmos Chem Phys, 14, 6867-6879, 2014.
769 Yang, L. F., Luo, H. H., Yuan, Z. B., Zheng, J. Y., Huang, Z. J., Li, C., Lin, X. H., Louie, P. K. K., Chen, D. H., and
770 Bian, Y. H.: Quantitative impacts of meteorology and precursor emission changes on the long-term trend
771 of ambient ozone over the Pearl River Delta, China, and implications for ozone control strategy, Atmos
772 Chem Phys, 19, 12901-12916, 10.5194/acp-19-12901-2019, 2019.
773 Yarnal, B.: Synoptic Climatology in Environmental Analysis A Primer, Journal of Preventive Medicine
774 Information, 347, 170-180, 1993.
775 Yin, Z. C., Cao, B. F., and Wang, H. J.: Dominant patterns of summer ozone pollution in eastern China and
776 associated atmospheric circulations, Atmos Chem Phys, 19, 13933-13943, 10.5194/acp-19-13933-2019,
777 2019.
778 Yue, X., Unger, N., Harper, K., Xia, X. G., Liao, H., Zhu, T., Xiao, J. F., Feng, Z. Z., and Li, J.: Ozone and haze
779 pollution weakens net primary productivity in China, Atmos Chem Phys, 17, 6073-6089, 10.5194/acp-
780 17-6073-2017, 2017.
781 Zhang, J. X., Gao, Y., Luo, K., Leung, L. R., Zhang, Y., Wang, K., and Fan, J. R.: Impacts of compound extreme
782 weather events on ozone in the present and future, Atmos Chem Phys, 18, 9861-9877, 10.5194/acp-18-
783 9861-2018, 2018.
784 Zhao, Z. J., and Wang, Y. X.: Influence of the West Pacific subtropical high on surface ozone daily variability
785 in summertime over eastern China, Atmos Environ, 170, 197-204, 2017.
786